Discrete iterative model and dynamical analysis of inductor current compensation on valley V^2 controlled boost converter

Haoyang Gan
Electrical Engineering dept.
Southwest Jiaotong University
Chengdu, P. R. China
ganhaoyang2008@163.com

Shengzhong He
Electrical Engineering dept.
Southwest Jiaotong University
Chengdu, P. R. China
szhe_0@swjtu.edu.cn

Minrui Leng
Electrical Engineering dept.
Southwest Jiaotong University
Chengdu, P. R. China
mrleng_pece@163.com

Fuban Qin
Electrical Engineering dept.
Southwest Jiaotong University
Chengdu, P. R. China
fuban_qin@163.com

***Abstract*—V^2 control has been widely used in voltage regulator module due to its fast transient response. However, for boost converter, conventional V^2 control cannot be applied. According to duality, valley V^2 control has been proposed and applied to control boost converter. But subharmonic oscillation exists when ceramic capacitor is used as output capacitor, due to its small output-capacitor time-constant. As nonlinear circuit, complex dynamical behaviors such as subharmonic oscillation and chaos exist in valley V^2 controlled boost converter. Adding inductor current as ramp compensation is an effective way to eliminate the instability. In this paper, to investigate the dynamical behavior and stabilization of inductor current compensation on valley V^2 controlled boost converter, discrete iterative model is established. Based on the model, the bifurcation behavior is observed as inductor current sensing coefficient increases. The orbit transfers from chaos to period-doubling bifurcations, and then to stable state. Experimental prototype is built up to verify the theoretical analysis. Both time-domain waveforms and phase portraits are consistent with bifurcation diagram. The instability mechanism is also analyzed by investigating loci of eigenvalues, so that stability boundary in operation regions is obtained.**

Keywords—inductor current compensation, valley V^2 control, discrete iterative model, boost converter, stability analysis

I. INTRODUCTION

High speed digital integrated circuit requires voltage regulator module (VRM) with fast load transient response [1]. V^2 control utilizes output voltage ripple as additional control variable so that transient response is improved [2]. Hence it has been popularly applied in VRM [3-5]. However, conventional V^2 control relies on peak value of output voltage ripple Δv_o. It hardly applied to boost converter whose Δv_o decreases after switch is turned on. In [6], valley V^2 control is proposed on basis of duality. In [7], valley V^2 controlled boost converter is discussed and critical equivalent series resistance (ESR) for stability is derived. With small time constant (ESR times capacitance) output capacitor like ceramic caps, instability issues exist like subharmonic oscillation and other dynamical phenomena [8-10]. But due to its small size and low cost, ceramic caps are popular in electronics products nowadays.

It's well known that ramp compensation is an efficient way to eliminate subharmonic oscillation. By introducing ramp voltage or current into the feedback of control loop, stable operation of converter can be extended [11]. In this paper, inductor current compensation [12] is chosen to stabilize valley V^2 controlled boost converter due to its simple sensing circuit compared with other methods like compensating by capacitor current [13], or external ramp [14]. It is also easier to implement compared with hybrid ramp [15] which combines both inductor current ramp and external ramp.

To investigate damping effect of inductor current compensation, dynamical analysis by discrete iterative modeling [8, 16-17] is adopted. It is more accurate then sampled-data modeling [18] and avoids calculating complicated monodromy matrix [19-20]. Moreover, compared with small signal analysis [14-15], bifurcation diagram obtained by discrete iterative model directly shows stability of converter as parameter varies in one diagram, which is more intuitive and convenient. Since previous work mainly focus on prediction of instability and stabilization for buck converter [12-15], less attention is paid on valley V^2 controlled boost converter, this work provides stabilization and parameter design for stable operation of the converter.

II. DISCRETE ITERATIVE MODEL

A. Operation Principle

Fig. 1(a) shows schematic diagram of valley V^2 controlled boost converter with inductor current compensation. The power stage consists of input voltage V_g, inductor L, switch S, diode D, output capacitor C with ESR r_e, and load R. In the outer control loop, error amplifier compares reference voltage V_{ref} with output voltage v_o, and then generates compensated error signal v_k, where $v_k = K(V_{ref} - v_o)$, K is the proportional coefficient of the error amplifier. In the inner loop, sensing voltage v_s not only contains output sensing voltage, but also compensated with inductor current sensing voltage $R_i \times i_L$, where R_i is inductor current sensing coefficient, i_L is inductor current. Thus $v_s = R_i \times i_L + K_v \times v_o$, where K_v is the output voltage sensing coefficient and $K_v = R_2 / (R_1+R_2)$.

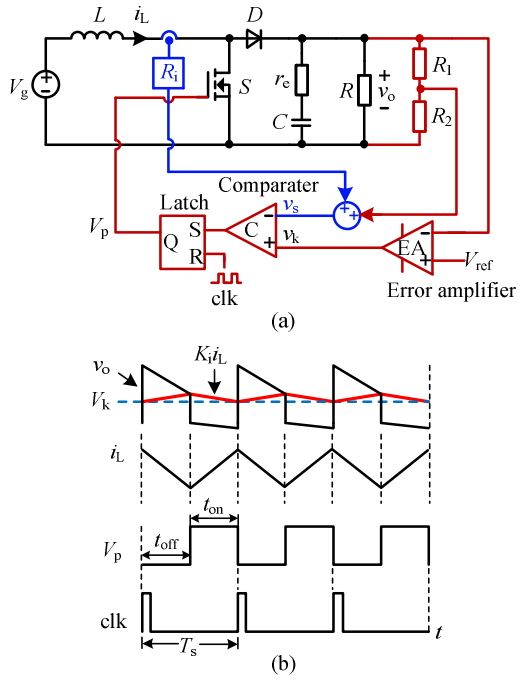

Fig. 1. Valley V^2 controlled boost converter with inductor current compensation. (a) Circuit schematic diagram. (b) Equivalent operation waveform.

When operating in stable continuous conduction mode (CCM), at the beginning of each switching cycle, switch S is turned off. Once $v_s = v_k$, switch S is turned on. Denoting V_k is the valley threshold voltage and K_i is equivalent inductor current sensing coefficient, the switched condition can be rewritten as

$$v_o = V_k + K_i i_L \tag{1}$$

where $V_k = \dfrac{K}{K_v + K} V_{ref}$ and $K_i = -\dfrac{R_i}{K_v + K}$.

Hence the equivalent operation waveform is plotted in Fig. 1(b), where clk is clock signal, V_p is the control pulse voltage, T_s is switching cycle, t_{off} is the off-time interval, t_{on} is the on-time interval. If there is no inductor current compensation, switch S will be turned on when output voltage decreases to valley threshold voltage. The compensated inductor current behaves like ramp compensation so S will change switching state when v_o decreases to $V_k + K_i \times i_L$.

There are two switch operation states when boost converter operates in CCM. State 1: S is on and D is off. State 2: S is off and D is on. By defining inductor current i_L and capacitor voltage v_c as state variables, the state equations of boost converter are deduced as follows:

$$\dot{\mathbf{x}} = \begin{cases} \mathbf{A}_1 \mathbf{x} + \mathbf{B}_1 V_g, & S:\text{on},\ D:\text{off} \\ \mathbf{A}_2 \mathbf{x} + \mathbf{B}_2 V_g, & S:\text{off},\ D:\text{on} \end{cases} \tag{2}$$

where $\mathbf{x} = [i_L \quad v_c]^T$, $\mathbf{A}_1 = \begin{bmatrix} 0 & 0 \\ 0 & \dfrac{-1}{(R+r_e)C} \end{bmatrix}$,

$\mathbf{A}_2 = \begin{bmatrix} \dfrac{-Rr_e}{(R+r_e)L} & \dfrac{-R}{(R+r_e)L} \\ \dfrac{R}{(R+r_e)C} & \dfrac{-1}{(R+r_e)C} \end{bmatrix}$, and $\mathbf{B}_1 = \mathbf{B}_2 = \begin{bmatrix} \dfrac{1}{L} & 0 \end{bmatrix}^T$.

B. Discrete Iterative Map

Denoting $\mathbf{x}_{(n)} = \mathbf{x}(nT_s)$, $\mathbf{x}_{(n+1)} = \mathbf{x}((n+1)T_s)$ are the values of state variables at the beginning of the n-th and the $(n+1)$-th switching cycle respectively, the discrete iterative map of valley V^2 controlled boost converter with inductor current compensation is expressed as the function between $\mathbf{x}_{(n)}$ and $\mathbf{x}_{(n+1)}$, i.e. $\mathbf{x}_{(n+1)} = f(\mathbf{x}_{(n)})$.

In the n-th switching cycle, the capacitor voltage v_c and inductor current i_L at $t = nT_s + t_{off}$ are solved from (2) as follows:

$$\begin{cases} v_c(nT_s + t_{off}) = e^{-\alpha t_{off}}(K_1 \sin \omega t_{off} + K_2 \cos \omega t_{off}) + V_g \\ i_L(nT_s + t_{off}) = \dfrac{1}{R} e^{-\alpha t_{off}}(K_3 \sin \omega t_{off} + K_4 \cos \omega t_{off}) + \dfrac{V_g}{R} \end{cases} \tag{3}$$

where $\omega = \sqrt{\dfrac{R}{\tau L} - \alpha^2}$, $\tau = (r_e + R)C$, $\alpha = \dfrac{L + Rr_e C}{2\tau L}$,

$K_1 = \dfrac{Ri_{L(n)} - v_{c(n)}}{\omega\tau} + \dfrac{\alpha}{\omega} K_2$, $K_2 = v_{c(n)} - V_g$,

$K_3 = K_1 - \tau(\alpha K_1 + \omega K_2)$, and $K_4 = K_2 - \tau(\alpha K_2 - \omega K_1)$.

The output voltage v_o is a function of capacitor voltage v_c and inductor current i_L, i.e.

$$v_o(t) = \frac{Rr_e}{R + r_e} i_L(t) + \frac{R}{R + r_e} v_c(t) \tag{4}$$

According to (1), when $v_o(nT_s + t_{off}) = V_k + K_i i_L(nT_s + t_{off})$, switch S is turned on, thus the switched condition function is

$$s(v_{o(n)}, t_{off}) = V_k + K_i i_L(nT_s + t_{off}) - v_o(nT_s + t_{off}) \tag{5}$$

Setting $s(v_{o(n)}, t_{off}) = 0$, t_{off} can be calculated by Newton's numerical iterative method. Comparing t_{off} with T_s, the discrete iterative map are divided into three cases, as shown in Fig. 2:

Case 1: $t_{off} \geq T_s$, switch S keeps the off-state throughout the switching cycle. By substituting $t_{off} = T_s$ into (3), the discrete iterative map is obtained.

Case 2: $0 < t_{off} < T_s$, switch S is turned off firstly, and then is turned on. The on-time interval is T_s - t_{off}, the discrete iterative map are deduced by substitute (3) into (2).

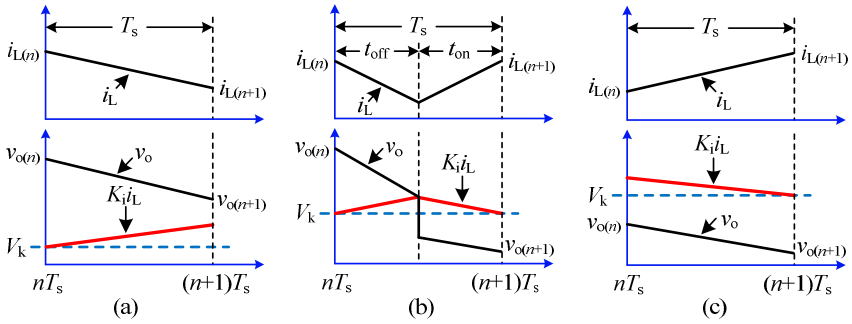

Fig. 2. Discrete iterative map of valley V^2 controlled boost converter with inductor current compensation. (a) $t_{off} \geq T_s$. (b) $0 < t_{off} < T_s$. (c) $t_{off} = 0$.

$$\begin{cases} v_{c(n+1)} = v_c(nT_s + t_{off})e^{\frac{-(T_s - t_{off})}{\tau}} \\ i_{L(n+1)} = \dfrac{V_g}{L}(T_s - t_{off}) + i_L(nT_s + t_{off}) \end{cases} \tag{6}$$

Case 3: $t_{off} = 0$, switch S keeps the on-state throughout the switching cycle. The discrete iterative map is

$$v_{c(n+1)} = v_{c(n)}e^{\frac{-T_s}{\tau}}, \quad i_{L(n+1)} = \frac{V_g}{L}T_s + i_{L(n)} \tag{7}$$

C. Maximal Lyapunov Exponent

The maximal Lyapunov exponent reflects stable state of the converter qualitatively. By solving Jacobian matrix of the converter, maximal Lyapunov exponent can be deduced. The Jacobian matrix of the converter is defined by

$$\mathbf{J}_n = \begin{bmatrix} J_{11} & J_{12} \\ J_{21} & J_{22} \end{bmatrix}\Bigg|_{\mathbf{x}_{(n)}} \tag{8}$$

where $J_{11} = \dfrac{\partial i_{L(n+1)}}{\partial i_{L(n)}}$, $J_{12} = \dfrac{\partial i_{L(n+1)}}{\partial v_{c(n)}}$, $J_{21} = \dfrac{\partial v_{c(n+1)}}{\partial i_{L(n)}}$, and $J_{22} = \dfrac{\partial v_{c(n+1)}}{\partial v_{c(n)}}$.

If $t_{off} \geq T_s$, elements of $\mathbf{J}_n$ are:

$$\begin{cases} J_{11} = \dfrac{e^{-\alpha T_s}}{R}\left[(1-\tau\alpha)\dfrac{R}{\tau\omega}\sin\omega T_s + R\cos\omega T_s\right] \\ J_{12} = \dfrac{e^{-\alpha T_s}}{R}\left[\dfrac{-(1-\tau\alpha)^2}{\tau\omega} - \tau\omega\right]\sin\omega T_s \\ J_{21} = e^{-\alpha T_s}\dfrac{R}{\tau\omega}\sin\omega T_s \\ J_{22} = e^{-\alpha T_s}\left[\left(-\dfrac{1}{\tau\omega} + \dfrac{\alpha}{\omega}\right)\sin\omega T_s + \cos\omega T_s\right] \end{cases} \tag{9}$$

If $0 < t_{off} < T_s$, elements of $\mathbf{J}_n$ are:

$$\begin{cases} J_{11} = \dfrac{\partial i_L(t_{off})}{\partial i_{L(n)}} - \dfrac{V_g}{L}\dfrac{\partial t_{off}}{\partial i_{L(n)}} \\ J_{12} = \dfrac{\partial i_L(t_{off})}{\partial v_{c(n)}} - \dfrac{V_g}{L}\dfrac{\partial t_{off}}{\partial v_{c(n)}} \\ J_{21} = e^{\frac{-(T_s - t_{off})}{\tau}}\left[\dfrac{\partial v_c(t_{off})}{\partial i_{L(n)}} + \dfrac{v_c(t_{off})}{\tau}\dfrac{\partial t_{off}}{\partial i_{L(n)}}\right] \\ J_{22} = e^{\frac{-(T_s - t_{off})}{\tau}}\left[\dfrac{\partial v_c(t_{off})}{\partial v_{c(n)}} + \dfrac{v_c(t_{off})}{\tau}\dfrac{\partial t_{off}}{\partial v_{c(n)}}\right] \end{cases} \tag{10}$$

If $t_{off} = 0$, elements of $\mathbf{J}_n$ are:

$$J_{11} = 1, \quad J_{12} = 0, \quad J_{21} = 0, \quad J_{22} = e^{\frac{-T_s}{\tau}} \tag{11}$$

Based on (8), Lyapunov exponents are calculated by

$$\begin{bmatrix} \lambda_{L1} \\ \lambda_{L2} \end{bmatrix} = \lim_{n\to\infty}\frac{1}{n}\ln\left|\mathrm{eig}\left(\prod_{k=1}^{n}\mathbf{J}_k\right)\right| \tag{12}$$

where $\mathbf{J}_k$ is Jacobian matrix evaluated along trajectory, $\mathrm{eig}\left(\prod_{k=1}^{n}\mathbf{J}_k\right)$ is a function to obtain eigenvalues of $\prod_{k=1}^{n}\mathbf{J}_k$.

Thus the maximal Lyapunov exponent is

$$\lambda_L = \max(\lambda_{L1}, \lambda_{L2}) \tag{13}$$

where max (λ_{L1}, λ_{L2}) is a function to get the maximal value between λ_{L1} and λ_{L2}.

III. Dynamical Behaviors and Stability Analysis

A. Dynamical Analysis

Equations (3) - (7) describe the discrete iterative model of

valley V^2 controlled boost converter with inductor current compensation. Denote initial state variable $\mathbf{x}_0$ is $[2, 1]^T$, and set circuit parameters as follows: V_g = 4V, L=150μH, C=1000μF, r_e=39mΩ, R=10Ω, V_{ref} =10.05V, K=20, K_v=0.1, T_s=50μs. Based on the model, when no inductor current compensation is applied, bifurcation diagram of ESR, r_e is shown in Fig. 3(a). The orbit of converter has a transition from stable period-1 to sequential period-doubling bifurcations and then to chaos as r_e decreases. When r_e = 39 mΩ, the converter is in chaos.

Utilizing inductor current compensation and taking R_i as bifurcation parameter, bifurcation diagram is shown in Fig. 4(a). As R_i increases, the orbit of converter transfers from chaos to period-doubling bifurcations, and then to period-1, which implies inductor current compensation has stability effect on valley V^2 controlled boost converter. The bigger R_i is, the better stability effect is. The first period-doubling bifurcation appears at R_i = 0.374, the second and third occurs at R_i = 0.038 and 0.012. When 0 < R_i < 0.007, the orbit is in chaos.

Calculated from (8) - (13), the maximal Lyapunov exponents of R_i are depicted in Fig. 4(b). As R_i increases, λ_L locates at positive at first, then goes down to negative at R_i = 0.007. When R_i = 0.012, 0.038, and 0.374 respectively, λ_L reaches zero from negative then back to negative again, consisting with each period-doubling bifurcation. Fig. 4(b) shows same dynamics as Fig. 4(a), verifying correctness of bifurcation diagram.

To compares more intuitive, when R_i = 0.2, for the same range of r_e, bifurcation diagram of r_e is depicted in Fig. 3(b). Only the first period-doubling bifurcation can be seen, and it appears at r_e = 47.6 mΩ. However in Fig. 3(a), the first period-doubling bifurcation occurs at r_e = 56.8 mΩ. The comparison demonstrates transition point of period-doubling bifurcation has been leftwards when inductor current compensation is used.

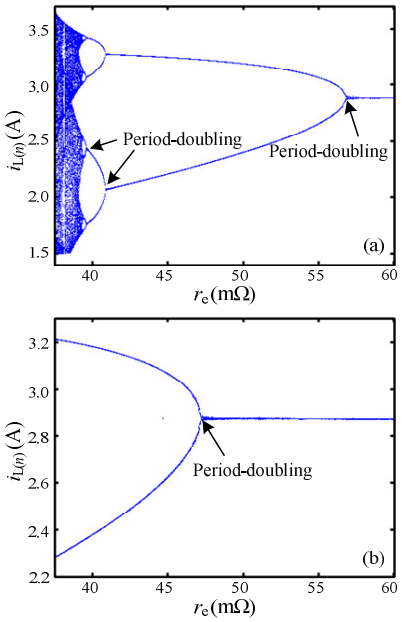

Fig. 3. Bifurcation diagrams with r_e as bifurcation parameter. (a) at R_i = 0. (b) at R_i = 0.2.

The stable operation range of r_e is also enlarged, showing the instability caused by small ESR has been stabilized by inductor current compensation.

B. *Instability Mechanism*

From above analysis, to stabilize the converter, R_i should bigger than 0.374. When R_i is less than 0.374, the converter loses stability. By investigating eigenvalues of Jacobian matrix around fixed point $\mathbf{X}_Q$ of the converter, the instability mechanism of R_i can be analyzed. When converter operates in equilibrium state, 0 < t_{off} < T_s, $\mathbf{X}_Q = [I_L\ V_c]^T$ can be solved by making $\mathbf{x}_{(n+1)} = \mathbf{x}_{(n)} = \mathbf{X}_Q$, where I_L and V_c are steady state inductor current and capacitor voltage at beginning of switching cycle respectively. By substitute $\mathbf{x}_{(n)} = \mathbf{X}_Q$ into (10), $\mathbf{J}_n(\mathbf{X}_Q)$ is obtained. The eigenvalues of $\mathbf{J}_n(\mathbf{X}_Q)$ can be calculated by solving the characteristic equation:

$$\det\left[\lambda\mathbf{I}-\mathbf{J}_n\left(\mathbf{X}_Q\right)\right]=0 \tag{14}$$

Table I shows eigenvalues of $\mathbf{J}_n(\mathbf{X}_Q)$ when R_i decreases from 0.4 to 0.35. The corresponding loci of eigenvalues are depicted in Fig. 5. There are two nonzero eigenvalues. As R_i decreases, one always locates inside unit circle, while another crosses unit circle via -1 from interior to exterior. Compared with Fig. 4(a), when two eigenvalues are all in unit circle, the converter is in stable period-1. Once the negative eigenvalue equals to -1, period-doubling bifurcation occurs, leading to loss of stability. Thus the stability boundary can be obtained by substituting λ = -1into (14), which is

$$J_{12}J_{21}-J_{11}J_{22}-J_{11}-J_{22}=1 \tag{15}$$

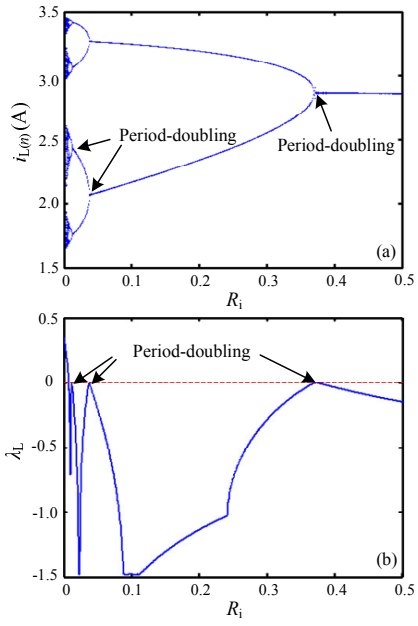

Fig. 4. Bifurcation diagram and maximal Lyapunov exponent λ_L as R_i increases.

TABLE I. EIGENVALUES OF $\mathbf{J}_n(\mathbf{X}_Q)$ AS R_i DECREASES

R_i	Eigenvalues	status in bifurcation diagram
0.400	-0.9802, 0.4645	Period 1
0.390	-0.9886, 0.4569	Period 1
0.380	-0.9925, 0.4518	Period 1
0.375	-0.9979, 0.4473	Period 1
0.374	**-1.0009,0.4455**	**Period-doubling bifurcation**
0.373	-1.0049, 0.4431	Period 2
0.370	-1.0365, 0.4256	Period 2
0.360	-1.0996, 0.3912	Period 2
0.350	-1.1408, 0.3690	Period 2

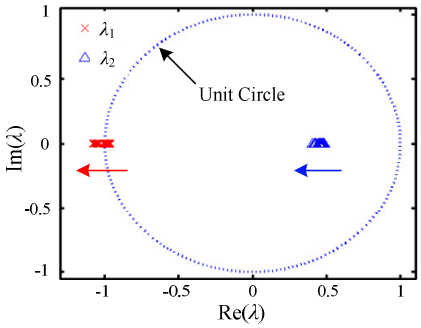

Fig. 5. Loci of eigenvalues as R_i decreases.(Arrow indicates the direction.)

Based on (15), stability boundary in parameter space R_i - re is plotted in Fig. 6, which divides operation regions into stable region and unstable region. Moreover, the stability boundary obtained by PSIM simulation is also plotted in Fig. 6, which is consistent with results obtained by boundary equation. The unstable region caused by small ESR decreases as R_i increases. The smaller ESR is, the greater R_i is needed to stabilize the instability.

IV. EXPERIMENTAL VERIFICATION

To verify bifurcation diagram, experimental prototype is built up. Differential sensing is used to perform the inductor current sensing. As Fig. 7 shows, ceramic capacitors are used. Switch S is IRF540N, diode is MBR1560CT, drive is IR2125,

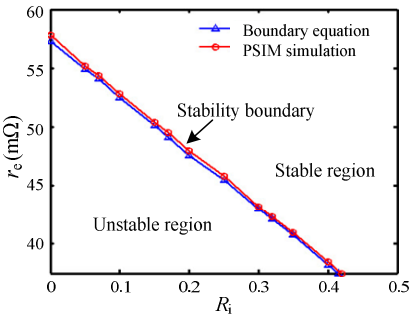

Fig. 6. Operation regions R_i - re.

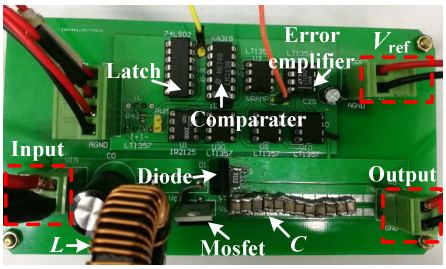

Fig. 7. Photograph of experimental prototype

error amplifier is LT1357, comparator is KA319, and latch is 74LS02. Time-domain waveforms and corresponding phase portraits under different R_i are captured in Fig. 8. Δv_o is output voltage ripple. When R_i = 0, time-domain waveforms are in chaos, there are a mass of orbits in phase portrait. When R_i = 0.3, converter operates in period-2, two orbits can be observed. When R_i = 0.5, converter operates in stable state, only one orbit appears. With increasing of R_i, chaos and subharmonic oscillation are eliminated, showing stability effect of inductor current compensation. The results well coincide with bifurcation diagram.

V. CONCLUSIONS

In this paper, inductor current compensation is utilized to stabilize valley V^2 controlled boost converter. Discrete iterative model is established to analyze dynamical behaviors. As inductor current sensing coefficient R_i increases, the orbit has

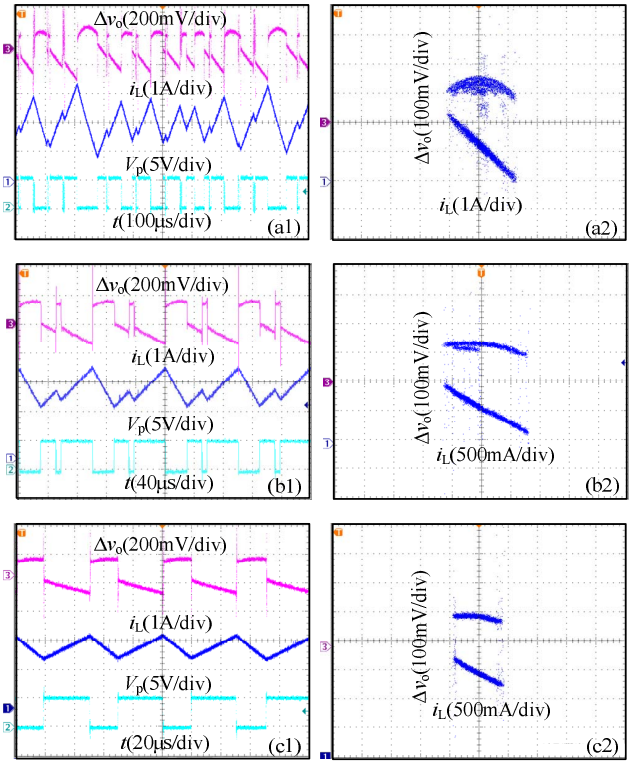

Fig. 8. Experimental time-domain waveforms and phase portraits with different R_i. (a) R_i = 0. (b) R_i = 0.3. (c) R_i = 0.5.

transitions from chaos to period-doubling bifurcations and then to period-1. Inductor current compensation eliminates subharmonic oscillation and chaos of the converter, verified by experiments. The instability mechanism is also investigated and stability boundary in operation regions is depicted, which provides guidelines for parameter design to stabilize valley V^2 controlled boost converter.

REFERENCES

[1] J. Sun, "Characterization and performance comparison of ripple-based control for voltage regulator modules," *IEEE Transactions on Power Electronics*, vol. 21, no. 2, pp. 346-353, Mar. 2006.

[2] R. Redl and J. Sun, "Ripple-based control of switching regulators—an overview," *IEEE Transactions on Power Electronics*, vol. 24, no. 12, pp. 2669-2680, Dec. 2009.

[3] Intel, VRM and EVRD 11.1 design guidelines, [Online], Available: https://www.intel.com/assets/PDF/designguide/321736.pdf.

[4] Texas Instruments, LM34919B datasheet, [Online], Available: http://www.ti.com.cn/cn/lit/ds/symlink/lm34919b.pdf.

[5] Texas Instruments, TPS51116 datasheet, [Online], Available: http://www.ti.com.cn/cn/lit/ds/symlink/tps51116.pdf.

[6] G. Zhou, J. Xu, J. Sha, and Y. Jin, "Valley V^2 control technique for switching converters with fast transient response," in *International Conference on Power Electronics - ECCE Asia*, 2011, pp. 2788-2791.

[7] G. Zhou, S. He, X. Chen, and H. Cui, "Can V^2 control be applied to boost converter," *Electronics Letters*, vol. 50, no. 8, pp. 627-629, Apr. 2014.

[8] S. He, G. Zhou, J. Xu, S. Wu, T. Yan, and X. Zhang, "Precise modeling and dynamic characteristics of valley V^2 controlled boost converter," *Acta Phys. Sin.*, vol. 63, no. 17, pp. 1-11, Sep. 2014. (in Chinese)

[9] X. Zhang, J. Xu, B. Bao, and G. Zhou, "Asynchronous-switching map-based stability effects of circuit parameters in fixed off-time controlled buck converter," *IEEE Trans. Power Electronics*, vol. 31, no. 9, pp. 6686-6697, Sep. 2016.

[10] S. K. Mazumder, A. H. Nayfeh, and D. Boroyevich, "Theoretical and experimental investigation of the fast- and slow-scale instabilities of a DC-DC converter," *IEEE Trans. Power Electronics*, vol. 16, no. 2, pp. 201-216, Mar. 2001.

[11] P. Yang, B. Bao, J. Sha, and J. Xu, "Dynamical mechanism of ramp compensation for switching converter," *Acta Phys. Sin.*, vol. 62, no. 1, pp. 010504-1-9, Jan. 2013. (in Chinese)

[12] J. Li and F. C. Lee, "Modeling of V^2 current-mode control," *IEEE Trans. Circuits and Systems I: Regular Papers*, vol. 57, no. 9, pp. 2552-2563, Sep. 2014.

[13] Y. Yan, P. H. Liu, F. Lee, Q. Li, and S. Tian, "V^2 control with capacitor current ramp compensation using lossless capacitor current sensing," in *2013 IEEE Energy Conversion Congress and Exposition*, 2013, pp. 117-124.

[14] S. Tian, F. C. Lee, P. Mattavelli, K. Y. Cheng, and Y. Yan, "Small-signal analysis and optimal design of external ramp for constant on-time V^2 control with multilayer ceramic caps," *IEEE Trans. Power Electronics*, vol. 29, no. 8, pp. 4450-4460, Aug. 2014.

[15] S. Tian, F. C. Lee, P. Mattavelli, and Y. Yan, "Small-signal analysis and optimal design of constant frequency V^2 control," *IEEE Trans. Power Electronics*, vol. 30, no. 3, pp. 1724-1733, Mar. 2015.

[16] M. Leng, G. Zhou, K. Zhang, and Z. Li, "Dynamics and stabilization of peak current-mode controlled buck converter with constant current load," *Chinese Physics B*, vol. 24, no. 10, pp. 100504-1-9, Oct. 2015.

[17] M. Leng, G. Zhou, S. Zhou, K. Zhang and S. Xu, "Stability analysis for peak current-mode controlled buck LED driver based on discrete-time modeling," *IEEE Journal of Emerging and Selected Topics in Power Electronics*, vol. 6, no. 3, pp. 1567-1580, Sep. 2018.

[18] S. Zhou, G. Zhou, S. Zeng, M. Leng, and S. Xu, "Sampled-data modeling and dynamical effect of output-capacitor time-constant for valley voltage-mode controlled buck-boost converter," *Chinese Physics B*, vol. 26, no. 11, pp. 118401-1-11, Nov. 2017.

[19] W. Hu, F. Zhang, X. Long, X. Chen, and W. Deng, "Stability analysis and control of nonlinear behavior in V^2 switching buck converter," *Journal of Power Electronics*, vol. 14, no. 6, pp. 1208-1216, Nov. 2014.

[20] J. Cortés, V. Šviković, P. Alou, J. A. Oliver, J. A. Cobos, and R. Wisniewski, "Accurate analysis of subharmonic oscillations of V^2 and V^2I_c controls applied to buck converter," *IEEE Trans. Power Electronics*, vol. 30, no. 2, pp. 1005-1018, Feb. 2015.